Dalton Transactions

ROYAL SOCIETY OF CHEMISTRY

PAPER

View Article Online
View Journal | View Issue

Cite this: *Dalton Trans.*, 2022, **51**, 9522

Preparation, characterization and DFT+U study of the polar Fe^{3+}-based phase $Ba_5Fe_2ZnIn_4S_{15}$ containing *S* = 5/2 zigzag chains†

Batoul Almoussawi, Victor Duffort, Angel M. Arevalo-Lopez, Maxime Braun, Nora Djelal and Houria Kabbour *

Received 8th March 2022,
Accepted 18th May 2022

DOI: 10.1039/d2dt00733a

rsc.li/dalton

The polar magnetic chalcogenide phase $Ba_5Fe_2ZnIn_4S_{15}$ was synthesized and its structure was solved by single crystal XRD. It is the first member with a 3d magnetic metal (Fe^{3+}) in the $Pb_5ZnGa_6S_{15}$-type structure family of wide bandgap materials with non-linear optical properties. The three-dimensional framework possesses a low dimensional magnetic character through the presence of weakly interacting zig-zag chains made of corner-sharing FeS_4 tetrahedra forming chain 1, $[FeS_2]^-_\infty$. The latter chains are separated by InS_4 tetrahedra providing weak magnetic super-super exchanges between them. The framework is also constituted by chain 2, $[In_3Zn_1S_9]^{7-}_\infty$ (chain of T2-supertetrahedra) extended similarly to chain 1 along the direction *c* and connected through InS_4 tetrahedra. Symmetry analysis shows that the intrinsic polarization observed in this class of materials is mostly due to the anionic framework. Preliminary magnetic measurements and density functional theory calculations suggest dominating antiferromagnetic interactions with strong super-exchange coupling within the Fe-chains.

Introduction

The interest in the search and study of transition metal chalcogenide compounds is due to their structural diversity and compositional complexity.[1] These characteristics lead to appealing properties.[2,3] For instance, superconductivity coexists with ferromagnetism in layered iron-based chalcogenide Cr-doped $FeTe_{0.8}S_{0.2}$.[4] Multiferroicity has also been found in several Fe-based systems.[5–7] On the other hand, polar chalcogenides with second harmonic generation (SHG) responses are being investigated for their nonlinear optical properties.

An interesting strategy to target new multiferroic phases is to substitute these strongly polar systems using magnetic cations in order to induce magnetic interaction on top of the polar distortion. Therefore, in this work, we focused on the polar structure type $A_5ZnM_6S_{15}$ with the reported members $Sr_5ZnGa_6S_{15}$ [8] and $Pb_5ZnGa_6S_{15}$ [9] phases (space group *Ama*2). They are wide bandgap semiconductors and exhibit a strong SHG response. Thus, we attempt to insert Fe^{3+} ($3d^5$, S = 5/2) providing strong magnetic coupling. They are characterized by interconnected Ga_4S_{10} T2-supertetrahedra, dimeric Ga_2S_7 tetrahedra and ZnS_4 tetrahedra to form a complex 3D non-centrosymmetric (NCS) anionic framework with a large cation residing in the irregular voids (Sr^{2+} or Pb^{2+} in the later examples). Here we have synthesized the first magnetic member $Ba_5Fe_2ZnIn_4S_{15}$. Besides, a few polar magnetic sulfides are found in the literature with Fe^{3+} as the magnetic ion, such as the chain compounds RE_3MInS_7 (RE = rare earth and M = Fe, Co, and Ni in an octahedral environment) related to the La_3CuSiS_7-type which exhibits antiferromagnetic interactions.[10] With other magnetic ions, one can cite the polar sulfide $Na_8Mn_2(Ge_2Se_6)_2$ which was mainly studied for its nonlinear optical properties and is a paramagnetic semiconductor.[11] The polar chalcogenides $BaLnSn_2Q_6$ (Ln = Ce, Pr, Nd and Q = S and Se) were reported as well with paramagnetic behaviour obeying the Curie–Weiss law.[12]

Here, we present the in-depth structural characterization of the polar magnetic chalcogenide $Ba_5Fe_2ZnIn_4S_{15}$, using multiple cations with different scattering factors to provide new insights into the chemical speciation of each cationic site. Symmetry analysis of the structure is used to emphasize the origin of the non-centrosymmetry and polarity of this structure type. Finally, a low dimensionality magnetism is proposed based on the preliminary magnetic study combined with DFT calculations.

Univ. Lille, CNRS, Centrale Lille, ENSCL, Univ. Artois, UMR 8181 – UCCS – Unité de Catalyse et Chimie du Solide, F-59000 Lille, France.
E-mail: houria.kabbour@univ-lille.fr

†Electronic supplementary information (ESI) available. CCDC 2148490. For ESI and crystallographic data in CIF or other electronic format see DOI: https://doi.org/10.1039/d2dt00733a

Experimental section

Synthesis

The synthesis was carried out with a stoichiometric mixture of the precursors $BaS/In_2S_3/Zn/Fe/S$. These precursors were mixed and thoroughly ground in an agate mortar before being pressed into pellets and heated in an evacuated sealed quartz tube. The heat treatment consisted of heating up to 1000 °C at a rate of 250 °C h^{-1} for 7 hours and then cooling down to 700 °C at a 30 °C h^{-1} rate, after which the furnace was switched off.

X-ray diffraction of single crystals was performed on an X8 diffractometer equipped with a bi-dimensional CCD 4 K detector and an Ag K_α source.

Mode symmetry analysis was performed using the ISODISTORT software[13] and the representation of the atomic shifts was drawn using the Vesta 3 software.[14]

The powder X-ray diffraction pattern was obtained on a Bruker D8 diffractometer equipped with a linear detector Lynxeye ($Cu_{K\alpha}$) in the Bragg–Brentano geometry at room temperature.

Magnetic measurements were performed on a 7 T Dynacool PPMS from Quantum Design by field cooled (FC) and zero field cooled (ZFC) procedures under an external field of 0.1 T.

DFT calculations were carried out by employing the projector augmented wave (PAW)[15,16] method encoded in the Vienna *ab initio* simulation package (VASP)[17] and the generalized gradient approximation of Perdew, Burke and Ernzerhof[18] (PBE) for the exchange–correlation functionals. A plane wave cutoff energy of 550 eV and a threshold of self-consistent-field energy convergence of 10^{-6} eV were used, with 74 k points in the irreducible Brillouin zone for the spin polarized GGA+U (U_{eff} = 4 eV) calculations of $Ba_5Fe_2ZnIn_4S_{15}$.

For the site preference calculations in $Sr_5ZnGa_6S_{15}$ and $Pb_5ZnGa_6S_{15}$, full geometry optimizations were carried out using a plane wave energy cutoff of 550 eV and 30 k points in the irreducible Brillouin zone. It converged with residual Hellman–Feynman forces on the atoms smaller than 0.03 eV $Å^{-1}$ and led to a good match with the experimental structure, *i.e.* within a reasonable error expected for the GGA method. The relaxed structure was used for calculations of the electronic structure. For the latter, a plane wave cutoff energy of 550 eV and a threshold of self-consistent-field energy convergence of 10^{-6} eV were used, with 90 k points in the irreducible Brillouin zone.

Scanning electron microscopy (SEM) experiments and EDX analysis were carried out on a Hitachi S400N.

Results and discussion

Structure solution and description

The structure (Fig. 1) was solved using single crystal XRD data (CCDC deposition number 2148490†) obtained from a black platelet crystal. It crystallizes in the orthorhombic system with cell parameters a = 23.4580(19) Å, b = 18.551(6) Å, and c = 6.464(5) Å and the polar space group *Ama*2 (40). The data collection and refinement details are given in Table 1. The

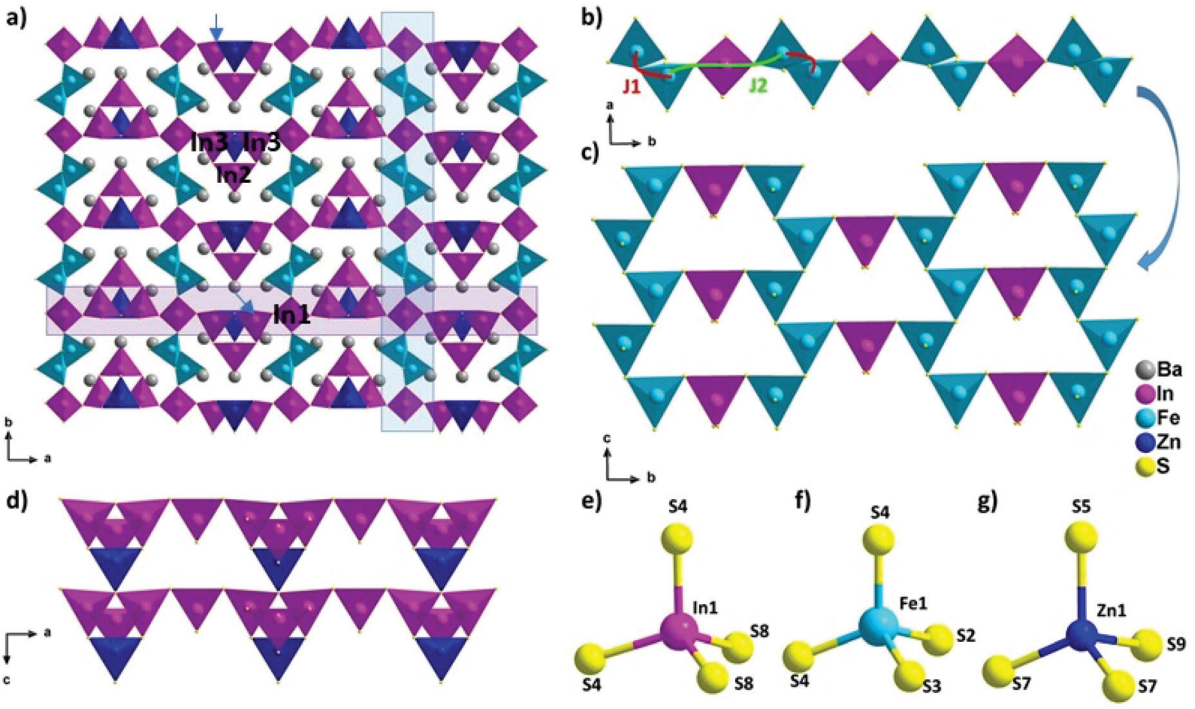

Fig. 1 (a) View of $Ba_5Fe_2In_4Zn_1S_{15}$ along the c axis, (b) magnetic exchange coupling $J1$ and $J2$ in the chains extended along the b axis, (c) interconnection between magnetic chains, (d) view of lined chains of type 2, and (e–g) In1, Fe1 and Zn1 coordination, respectively.

Table 1 Refinement parameters of $Ba_5Fe_2In_4ZnS_{15}$

Formula	$Ba_5Fe_2In_4ZnS_{15}$
Molecular weight (g mol^{-1})	1804
Symmetry	*Orthorhombic*
Space group	*Ama*2 (40)
Unit cell dimensions (Å)	a = 23.458(2)
	b = 18.551(6)
	c = 6.464(5)
Volume (Å^3)	2813(2)
Z	4
Data collection	
Equipment	Bruker CCD
λ [Ag K$_\alpha$; Å]	0.56087
Calculated density (g cm^{-3})	4.2599
Crystal shape	Platelet
Crystal dimensions (μm)	65 × 50 × 5
Color	Black
Absorption correction	Analytical
Scan mode	ω, ϕ
θ (min–max) (°)	1.73–19.72
μ (mm^{-1}; for λ Kα = 0.56087 Å)	6.841
F(000)	3192
Reciprocal space recording	$-28 \le h \le 28$
	$-22 \le k \le 22$
	$-7 \le l \le 7$
No. of measured reflections	37 736
No. of independent reflections	2633
$I > 3\sigma(I)$ (total)	2325
Refinement	
Number of refined parameters	245
Refinement method	Least-squares
Weighting scheme	Sigma
$R_1(F)$ $[I > 3\sigma(I)]/R_1(F^2)$ (all data, %)	0.0315/0.0382
w$R_2(F^2)$ $[I > 3\sigma(I)]$/w$R_2(F^2)$ (all data, %)	0.0374/0.0386
Goodness of fit	1.42
Flack parameter	0.05(5)
Max/Min residual electronic density (e$^-$/Å^3)	1.39/−1.86
T_{min}/T_{max}	0.6607/0.7387

refinement was carried out using the JANA2006[19] software based on a structure solution obtained using the charge flipping method.[20] The EDS analysis of the single crystals (Fig. 2) revealed an average atomic ratio of 19.6/8.6/3.8/11.0/57.1 for Ba/Fe/Zn/In/S. This is in good agreement with the theoretical ratio expected for the refined formula $Ba_5Fe_2ZnIn_4S_{15}$, *i.e.* 18.5/7.4/3.7/14.8/55.6 for Ba/Fe/Zn/In/S. In particular, the Fe ratio is about twice the Zn ratio which is consistent with their refined distribution.

The new phase $Ba_5Fe_2ZnIn_4S_{15}$ is a 3D framework (Fig. 1, Tables 2–5) combining three different types of tetrahedra InS_4, FeS_4 and ZnS_4 (Fig. 1e, f and g). The standard description of this family has been reported for several non-magnetic chalcogenides, *e.g.* SHG active compounds $Sr_5ZnGa_6S_{15}$ and $Pb_5Ga_6ZnS_5$ with wide bandgaps.[8,9] The atomic positions are very close to those reported in the previous compositions with the exception of the zinc position, as discussed later. Please note that due to the polar nature of the space group, multiple origin choices are possible. The transformation matrices to apply in the reported atomic positions[8,9] for straightforward comparison can be found in Table S1.†

The structural model can be described as the stacking of two distinct 1D building blocks. The $[FeS_2]^-_\infty$ zigzag chain (1) extending along the c axis is built from corner-sharing $[Fe1S_4]^{5-}$ tetrahedra (Fig. 1c) and the T2 supertetrahedron (made of 4 tetrahedra forming M_4X_{10} with M as the cation and X as the anion) based chain (2) $[In_3Zn_1S_9]^{7-}_\infty$ which also extends along the c axis (Fig. 1d). In the latter chain, the corner sharing $[In_3ZnS_{10}]^{8-}$ T2-supertetrahedra are composed of one $[In2S_4]^{5-}$, two $[In3S_4]^{5-}$ and one $[Zn1S_4]^{6-}$ tetrahedra. In the FeS_4 tetrahedra, the distances d_{Fe-S} are found to be between 2.238 Å and 2.266 Å and lead to a BVS of 3.02(5) which is consistent with the Fe^{3+} oxidation state calculated from the charge balance. This range is comparable to the one reported for instance in $Ba_5Fe_4S_{11}$ which also has Fe^{3+} in the FeS_4 tetrahedra, with $d(Fe^{3+}–S^{2-})$ = 2.214–2.306 Å.[21] The In–S bond lengths ranging from 2.377 Å to 2.484 Å are comparable

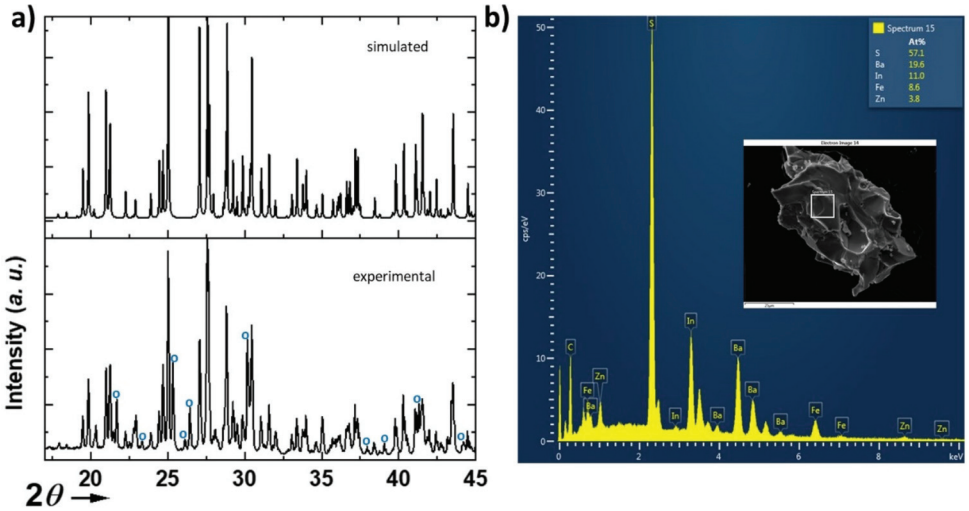

Fig. 2 (a) X-ray diffraction pattern of $Ba_5Fe_2In_4ZnS_{15}$ calculated from single crystal refinement, and compared to the X-ray experimental pattern of the obtained powder; impurity peaks are indexed to blue circles. (b) EDX analysis with atomic ratios and SEM image of a crystal (inset).

Table 2 Atomic positions and isotropic thermal displacement for $Ba_5Fe_2In_4Zn_1S_{15}$

Atom	Wyck.	*x*	*y*	*z*	U_{eq}
Ba1	4b	3/4	0.34541(7)	0.147(2)	0.0128(4)
Ba2	8c	0.61457(3)	0.13332(2)	0.068(2)	0.0110(2)
Ba3	8c	0.10987(3)	0.16031(4)	0.102(2)	0.0126(2)
In1	4a	1/2	1/2	0.078(2)	0.0118(4)
In2	4b	3/4	0.69547	0.183(2)	0.0125(4)
In3	8c	0.66016(4)	0.5262(2)	0.055(2)	0.0203(3)
Fe1	8c	0.47101(7)	0.6962(1)	0.130(2)	0.0071(5)
Zn1	4b	3/4	0.52836(12)	0.531(2)	0.0079(6)
S1	4b	3/4	0.8245(3)	0.142(2)	0.0122(14)
S2	8c	0.37633(11)	0.69643(16)	0.088(2)	0.0100(9)
S3	8c	0.51069(14)	0.70254(19)	−0.186(2)	0.0125(10)
S4	8c	0.49966(15)	0.60120(19)	0.323(2)	0.0125(10)
S5	4b	3/4	0.6575(2)	0.551(2)	0.0112(13)
S6	8c	0.65417(12)	0.65980(17)	0.066(2)	0.0121(9)
S7	8c	0.66700(13)	0.47875(19)	0.391(2)	0.0133(10)
S8	8c	0.58174(14)	0.4932(2)	−0.158(2)	0.0137(11)
S9	4b	3/4	0.4937(3)	−0.113(2)	0.0143(15)

to the range of bond lengths in $Ba_2In_2S_5$ [21] (from 2.386 Å to 2.503 Å). The Ba^{2+} cations are localized in the voids.

The two chains are interconnected *via* $[In1S_4]^{5-}$ tetrahedra along the *a* and *b* axis respectively to form the three-dimensional framework of the structure (Fig. 1a). The heterogeneous cation composition of the T2-supertetrahedra, *i.e.* $[In_3ZnS_{10}]^{8-}$, is observed for the first time. In previous studies on this structure type (ref. 8 and 9), the $[ZnS_4]^{6-}$ tetrahedron was reported as the connecting unit between the two chains that were composed purely of $[GaS_4]^{5-}$ tetrahedra. We would like to emphasize here that Zn^{2+} and Ga^{3+} being isoelectronic species, X-rays crystallography is a poor tool to resolve the chemical composition of Ga/Zn sites and therefore such structures are possibly ambiguous. Yet, the chemical speciation of the different sites is not discussed in previous studies. While our composition only has Zn^{2+} as the common cation with the other two previously reported structures, the atomic positions are remarkably similar. Therefore, the speciation information obtained in the case of $BaZnFe_2In_4S_{15}$, thanks to the different electron counts in Fe^{3+}, Zn^{2+} and In^{3+}, could also be relevant to help resolve the natural ambiguity of the Ga/Zn speciation in the other two structures.

Recently, the IR NLO phase $Ba_5CdGa_6Se_{15}$ with a strong SHG response has also been reported[22] with the $Pb_5ZnGa_6S_{15}$-type structure. In this phase there is no ambiguity concerning the repartition of Cd/Ga, but interestingly they suggest a site preference (4*a* site) for Zn in the parent phase $Pb_5ZnGa_6S_{15}$ without excluding Zn/Ga disorder.

In our study, reinvestigation of the reported structures of $Pb_5ZnGa_6S_{15}$ and $Sr_5ZnGa_6S_{15}$ shows evidence of a Zn/Ga inversion. In particular, in both structures the thermal displacement of Zn^{2+} is significantly smaller than that of other cations while the thermal parameter of the Ga site corresponding to the location of the Zn site in our structure is the largest of all Ga^{3+} cations. While all reported parameters are

Table 3 Distances, angles and number of magnetic exchange couplings between iron atoms

	Atom 1	Atom 2	*d*[1,2] (Å)	Fe–S–Fe (Å)	Fe–S···S–Fe (Å)	Fe–S–Fe (°)	Number of coupling
*J*1	Fe1	Fe1	4.0349(149)	Fe–S3 = 2.2478(167)		126.8*(4)*	2 + 8/2 = 6
*J*2	Fe1	Fe1	6.464(57)		Fe1–S7 = 2.265(5) S7–S7 = 3.7094(67)		16/2
*J*3	Fe1	Fe1	7.4054(35)		Fe1–S4···S4–Fe1 Fe–S4 = 2.2614(106) S4–S4 = 3.7548(5)		1 + 9/2 = 5.5

Table 4 Anisotropic thermal parameters U_{ij} (Å^2) for $Ba_5Fe_2In_4Zn_1S_{15}$

Atom	U_{11}	U_{22}	U_{33}	U_{12}	U_{13}	U_{23}
Ba1	0.0048(5)	0.0219(7)	0.0116(7)	0.0000(0)	0.0000(0)	0.0002(5)
Ba2	0.0075(3)	0.0119(4)	0.0136(5)	0.0006(3)	0.0016(4)	−0.0010(4)
Ba3	0.0081(3)	0.0193(4)	0.0105(5)	−0.0001(3)	0.0006(4)	−0.0027(4)
In1	0.0110(6)	0.0133(7)	0.0112(7)	−0.0004(5)	0.00000	0.00000
In2	0.0084(6)	0.0123(8)	0.0169(8)	0.000000	0.00000	0.0014(6)
In3	0.0194(5)	0.0229(6)	0.0187(6)	0.0010(4)	−0.0019(5)	0.0003(6)
Fe1	0.0044(8)	0.0100(10)	0.0069(10)	−0.0004(7)	0.0007(8)	−0.0002(8)
Zn1	0.0046(9)	0.0120(11)	0.0072(13)	0.000000	0.000000	−0.0008(9)
S1	0.008(2)	0.015(3)	0.014(3)	0.000000	0.000000	0.003(2)
S2	0.0031(13)	0.0142(16)	0.0127(18)	−0.0009(11)	−0.0011(15)	−0.0018(18)
S3	0.0128(17)	0.0128(19)	0.0118(19)	−0.0004(14)	0.0050(14)	0.0038(16)
S4	0.0110(15)	0.0120(19)	0.0144(19)	0.0031(12)	−0.0032(14)	0.0014(15)
S5	0.0065(19)	0.013(2)	0.014(3)	0.000000	0.000000	0.000(2)
S6	0.0100(14)	0.0135(16)	0.0129(18)	−0.0004(12)	−0.0043(15)	−0.0005(19)
S7	0.0111(16)	0.0161(19)	0.0127(19)	−0.0021(14)	0.0004(15)	0.0016(16)
S8	0.0112(16)	0.015(2)	0.0147(19)	−0.0014(14)	0.0062(15)	−0.0016(16)
S9	0.008(2)	0.022(3)	0.012(3)	0.000000	0.000000	0.003(2)

Table 5 Main distances (Å) for $Ba_5Fe_2In_4Zn_1S_{15}$

Atoms 1,2	*d* 1,2 [Å]	Atoms 1,2	*d* 1,2 [Å]
Ba1–S1	3.29(2)	In1–S4	2.454(13)*2
Ba1–S1	3.22(2)	In1–S8	2.456(12)*2
Ba1–S2	3.087(4)*2	In2–S1	2.407(6)
Ba1–S9	3.224(11)	In2–S5	2.484(19)
Ba2–S2	3.168(4)	In2–S6	2.461(6)*2
Ba2–S3	3.179(10)	In3–S6	2.417(4)
Ba2–S4	3.184(10)	In3–S7	2.380(18)
Ba2–S5	3.210(1)	In3–S8	2.395(11)
Ba2–S7	3.323(8)	In3–S9	2.463(9)
Ba2–S8	3.236(11)	Fe–S2	2.237(4)
Ba3–S1	3.309(2)	Fe1–S3	2.246(18)
Ba3–S2	3.232(19)	Fe1–S3	2.265(11)
Ba3–S3	3.239(9)	Fe1–S4	2.263(11)
Ba3–S4	3.324(11)	Zn1–S5	2.399(5)
Ba3–S7	3.209(9)	Zn1–S7	2.335(8)*2
Ba3–S8	3.310(10)	Zn1–S9	2.387(19)

within an acceptable range, this is exactly the effect one would expect if a slightly larger Zn^{2+} was squeezed in a Ga^{3+} position and *vice versa*. Finally, the hypothesis of Ga/Zn in previously reported structures was probed using geometry optimization by DFT calculations. In both $Pb_5ZnGa_6S_{15}$ and $Sr_5ZnGa_6S_{15}$, the energy of the optimized structure (see Tables S2–S5†) is significantly lower when the $[ZnS_4]^{6-}$ tetrahedron is part of the T2-supertetrahedra (−461.5 eV and −491.4 eV respectively) rather than in the reported position (−460.1 eV and −488.5 eV respectively).

None of the above elements are direct proof of the Zn position in $(Pb,Sr)_5ZnGa_6S_{15}$; however, we report here clear evidence that this question is still pending. It should be addressed with caution until powders with sufficient purity or large enough single crystals for neutron diffraction can be obtained.

Origin of the non-centrosymmetry and the polarization of the structure

With at least three compositions with the same structure type, sulphides with the $A_5ZnM_6S_{15}$ stoichiometry appear as a very promising family for the discovery of new polar materials. Understanding of the geometrical origin of the spatial inversion breaking appears as a critical element to improve the properties of these materials. To visualize the origin of the non-centrosymmetry and polarity observed in $A_5ZnM_6S_{15}$, we constructed a hypothetical centrosymmetric high-symmetry structure (aristotype) and used symmetry mode analysis[23] to decompose the atomic shifts, relating the aristotype to the lower-symmetry structure (hettotype), into centrosymmetric and non-centrosymmetric displacements.

Looking at the cationic framework of $Ba_5Fe_2ZnIn_4S_{15}$, we found that the structure is composed of 8 layers along *a*, 6 along *b* and only 2 along *c*. The positions of each cation can therefore be rounded off to the closest fractional coordinate with the form (n_x/8, n_y/6, n_z/2) to construct a high symmetry structure. The resulting arrangement has the *Cmcm* (#63) centrosymmetric space group; note that to avoid permutation of the basis vectors when transforming the aristotype to the hettotype, the non-standard setting *Amam* (#63-4) is used in the rest of the article. Similarly, the anion framework can be described using 8 layers along *a*, 6 along *b* and 4 along *c*, and the resulting atomic positions, also compatible with the *Amam* space group, are listed in Table S6.†

The decomposition of the different modes and the evaluation of their amplitude (Table S7†) were achieved using the ISODISTORT software (ref. 10). The 43 modes belong to two irreducible representations Γ_{1+} and Γ_{3-} with isotropic subgroups *Amam* and *Ama*2, respectively. This allows the differentiation between the atomic shifts breaking the inversion symmetry, *i.e.* belonging to Γ_{3-}, and the displacements compatible with the inversion center, *i.e.* belonging to Γ_{1+}. By applying the atomic shifts of the Γ_{1+} irreducible representation to the aristotype we can generate the best possible centrosymmetric model and represent the remaining atomic shifts using arrows (Fig. 3a). It is then easy to visualize that it is mostly the anionic framework that breaks the inversion symmetry. The cations have atomic shifts less than 0.4 Å with respect to the centrosymmetric *Amam* structure, with the exception of In2 that shows a shift of about 0.7 Å. Positions S3, S4, S7, S8 and S9 require a displacement greater than 1 Å to reach their actual position with a maximum of 1.2 Å for S9.

Because In1 lies on an inversion center in the aristotype structure, the deviation from a centrosymmetric structure is most obvious in the evolution of its coordination polyhedra (Fig. 3c). The pseudo-cubic environment imposed by the inversion center can be relaxed into a tetrahedral environment by pulling in atoms that are on the diagonal of each face since S3/S4 and S7/S8 are no longer equivalent positions in the *Ama*2 space group. Then, using the centrosymmetric and non-centrosymmetric models, the calculated polarization *via* point charge is found to be high with a value of 63.7 μC cm^{-2}.

The polarity of the structure, on the other hand, originates from the displacements along the polar axis, *c*. In this regard, the evolution of the T2 super-tetrahedral subunit (Fig. 3b) is much more relevant. The large shift of the S9 position along *c* is only partially compensated by a much smaller shift of the In1 position in the opposite direction. Several substitution strategies can then be devised to increase the polarization of this structure type. In particular, the effective charge carried by the anion in the S9 position is maximized by increasing the ionicity of its chemical bonds.

DFT calculations

The magnetic interactions within the title phase were investigated using DFT+U calculations at the GGA level. We have investigated several magnetic configurations using U_{eff} = 4 eV which is in the typical range of similar systems.[24] The structure was not relaxed to avoid slight geometrical changes in the spin chain that may affect the results.

Using the energy mapping analysis[25] and the magnetic configurations presented in (Fig. 4), we extracted from our DFT+U calculations the magnetic interaction constants *J*1, *J*2 and *J*3 (Table 3) (Fig. 5). We consider decoupled 2D layers containing

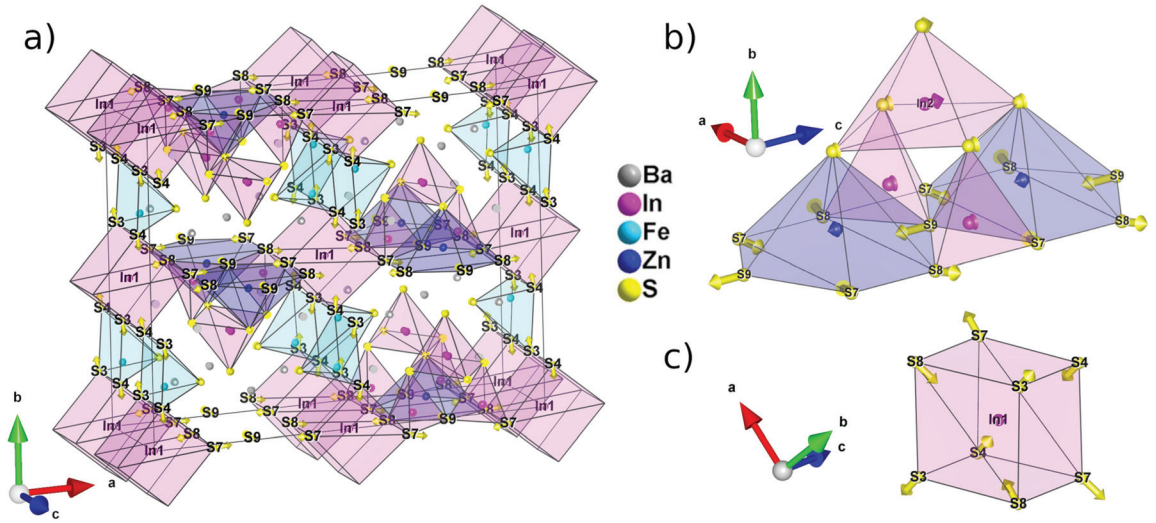

Fig. 3 Representation of the centrosymmetric (*Amam*) hypothetical aristotype of $Ba_5ZnFe_2In_4ZnS_{15}$ and the atomic shifts necessary to derive the real structure. The arrows representing the atomic displacements are drawn to scale meaning that the tip of the arrows points to the real position of the atoms. The position identification refers to the *Ama*2 cell. (a) Whole cell, (b) T2 super-tetrahedral subunit and (c) coordination sphere of In1.

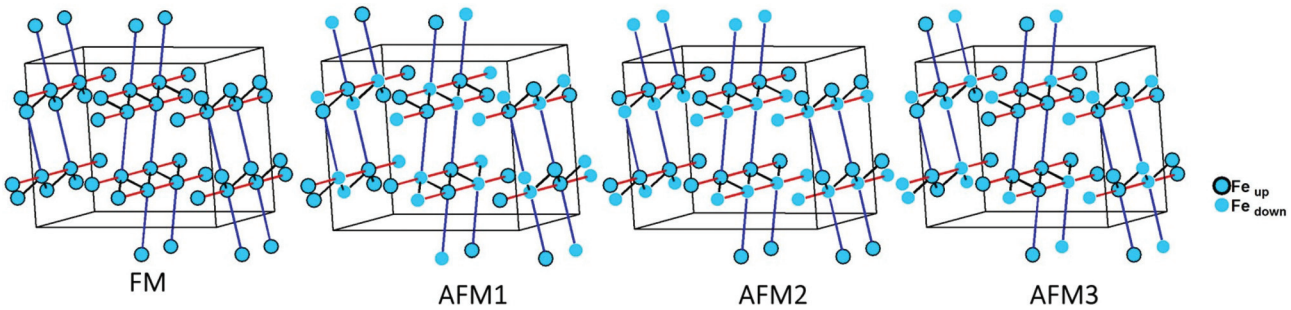

Fig. 4 Different magnetic configurations of $Ba_5Fe_2In_4Zn_1S_{15}$ used in the DFT+U calculations; *J*1, *J*2 and *J*3 are represented in black, red and blue, respectively.

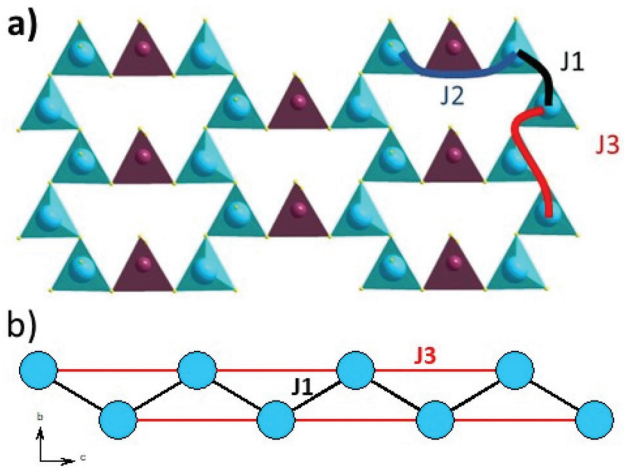

Fig. 5 (a) Magnetic exchange coupling scheme of *J*1, *J*2 and *J*3 between iron atoms. (b) Quasi one-dimensional zigzag magnetic chain built from iron atoms in blue with *J*1 and *J*3 intra-chain magnetic exchanges represented in black and red, respectively.

the spin chains weakly interacting. Based on the geometrical configuration we can propose and estimate a super-exchange mechanism within the chains (intra-chain, *J*1 coupling) and a super-super exchange mechanism between the chains (inter-chains couplings) as well as for the next-nearest neighbour interaction within the chains (*J*2 and *J*3 respectively). Another inter-chain path exists through the T2 supertetrahedra but is not considered due to its exceedingly long inter-chain distance (a path of four successive InS_4 tetrahedra between Fe atoms) providing a complete structural disconnection.

E_0: sum of the nonmagnetic parts.

J_{ij}: the exchange interactions between spin S_i and S_j at sites i and j, respectively.

The positive (negative) J_{ij} represents FM (AFM) coupling. For one formula unit, the total energies associated with different magnetic orders can be calculated using:

$$E_{(\mathrm{FM})} = E_0 - 16J1S^2 - 8J2S^2 - 16J3S^2 \quad (1)$$

$$E_{(\mathrm{AFM1})} = E_0 + 8J2S^2 + 16J3S^2 \quad (2)$$

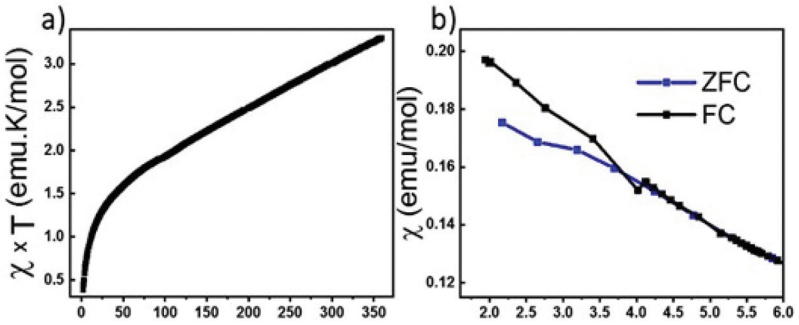

Fig. 6 (a) Temperature dependence of magnetic susceptibility χ_x *T*. (b) Zoom-in view of ZFC/FC at low temperature.

$$E_{(\mathrm{AFM2})} = E_0 + 16J1S^2 + 8J2S^2 - 16J3S^2 \quad (3)$$

$$E_{(\mathrm{AFM3})} = E_0 - 8J2S^2 + 8J3S^2 \quad (4)$$

Here, we use S = 5/2, accordingly with the charge of Fe assumed in this work (d^5) corresponding to high spin Fe^{3+}. The latter allows the J calculations using a defined spin state on each site. Using the equations above and the energies of the magnetic configurations presented in (Fig. 4), we extracted from our DFT+U calculations the magnetic interactions constants $J1$ = −206 K, $J2$ = −9.08 K and $J3$ = −6.62 K, considering U_{eff} = 4 eV. The DFT calculated local magnetic moment on the Fe sites is found to be around 3.9μ_B with slight variations depending on the magnetic configuration; such a value agrees with a high spin state of Fe^{3+}. All J couplings are found to be antiferromagnetic but $J1$ is largely dominating which avoids any competition between $J1$ and $J3$ (both in-chains and cannot be AFM at the same time) with $|J1| \gg |J3|$. $J2$, inter-chain, is also very weak compared to $J1$ and in the same range than $J3$. Therefore, this system can be described as an S = 5/2 AFM spin chain. For such a low dimensional magnetic system with highly disconnected 2D magnetic layers made of weakly interacting spin chains (with the strong $J1$ in chain), a clear establishment of a long-range magnetic ordering may not occur. Considering the large value of $J1$, we should keep in mind that it would be affected by U_{eff} applied for the calculations. We cannot adjust more accurately the U_{eff} value in the absence of experimental magnetic data on a pure sample (see the discussion below) to compare with the calculation results. Nevertheless, the trend and the dominating $J1$ are clear. Then, the large value of $J1$ may be related to the high spin configuration of d^5 (Fe^{3+}) which provides a maximal spin-only magnetic moment thus enabling greater magnetic interactions between the spin sites. Additionally, the role of the more covalent bonding with the sulfide anions (compared to oxides) should be further investigated. It is difficult to make a straightforward comparison with other systems but one can cite Ba_2FeS_3 with quasi one-dimensional (1D) spin chains built with corner sharing FeS_4 as found in our phase but not in a zigzag manner and with Fe^{2+} (S = 2) instead of Fe^{3+} (S = 5/2). In these cases, a long-range antiferromagnetic transition is found at 54 K (56 K, for a similar high pressure (HP) phase). In the latter phases, the intrachain coupling J_{intra} is calculated as −24 K (−18 K for HP) from the Wagner-Friedberg model.[26] In the centrosymmetric compound $BaFe^{3+}{}_2S_4$, the AFM 1D chains are made of $Fe^{3+}S_4$ with AFM SE but through edge-sharing, it exhibits a magnetic susceptibility which fits a classical S = 5/2 Heisenberg Hamiltonian.[27]

Powder sample and magnetic measurements

We have attempted to synthesize a pure powder phase. Numerous efforts allowed the increase of the purity of the sample and the powder XRD pattern of our best sample is presented in (Fig. 2). An impurity that could not be indexed to known phases persists. Although the title phase is the major phase as shown in the simulated and superimposed XRD pattern, the impurity is significant which makes the magnetic characterization and its interpretation difficult. Nevertheless, we have carried out a preliminary study.

Fig. 6 shows the temperature dependence of the magnetic susceptibilities. At around 2–3 K, a slight divergence of the ZFC/FC is observed; however it is difficult to attribute it to a specific phenomenon such as a spin glass state, low dimensional short-range magnetic correlations and/or a complex long-range magnetic order because of the significant amount of the unidentified impurity. Considering the DFT calculations which suggest that this system can be described as a low dimensional magnetic system (S = 5/2 AFM spin chain), the expected susceptibility for such behaviour would be a broad maximum; however the presence of the impurity hampers its observation. As shown in the ESI (Fig. S1†), we attempted fitting the magnetic susceptibility which shows AFM interactions dominating but it is impossible to fully interpret the magnetic data with the amount of unidentified impurity.

Conclusion

We describe here the synthesis and the structural and physical characterization of the new sulfide material $Ba_5Fe_2ZnIn_4S_{15}$. It adopts a polar structure type isostructural with a family of wide bandgap SHG materials, $A_5ZnM_6S_{15}$, containing chains of T2-supertetrahedra and $[MS_2]_\infty$ chains made of corner-sharing tetrahedra. The multi-element substitution on the M-site, M =

In and Fe, allowed us to gain insights into the chemical speciation of each cationic site highlighting the ambiguities in previously reported structures with the same structure type. In the title phase, the magnetic high-spin Fe^{3+} (d^5) transition metal lies in the $(MS_2)_\infty$ chains and the Zn^{2+} cation is part of the T2 super-tetrahedra. In-depth symmetry analysis of the structure shows that the intrinsic polarization observed in this class of materials is mostly due to the anionic framework and most particularly due to the S9 site.

A powder sample could be obtained but a significant unidentified impurity hampers deep physical characterization. Preliminary magnetic measurements reveal a divergence of the ZFC/FC at a very low temperature around 3 K and dominant antiferromagnetic interactions. DFT calculations suggest a stable antiferromagnetic state with strong AFM intrachain Fe–S–Fe super exchanges and very weak interchain Fe–S–S–Fe coupling (*via* InS_4). It thus represents an AFM $S = 5/2$ spin chain system. A pure powder and magnetic measurements based on single crystals are required to further investigate this sample. It represents a promising platform to measure electric polarization and tune the magnetic interactions toward multiferroic systems.

Conflicts of interest

There are no conflicts to declare.

Acknowledgements

This study was supported by the French government through the Programme Investissement d'Avenir (I-SITE ULNE/ANR-16-IDEX-0004 ULNE) managed by the Agence Nationale de la Recherche (Project ANION-COMBO). X-rays diffractometers were funded by Région NPDC, FEDER, CNRS and MESR. The regional computational cluster supported by Lille University, CPER Nord-Pas-de-Calais/CRDER, France Grille CNRS and FEDER is acknowledged for providing computational resources.

References

1 A. Abudurusuli, K. Wu, J. Li, A. Yalikun, Z. Yang and S. Pan, *LiBa 2 M*, 2019, vol. 4. DOI: **10.1021/acs.inorgchem.9b01810**.

2 N. Nakayama, *Studies on the Compounds in the Ba-Fe-S Antiferromagnetism of Ba, FeS, and Related System. I. Linear Chain Compounds Ba & OS*, 1980, vol. 356, pp. 351–356.

3 J. T. Lemley, *Ba, Fe, S, and Ba, FeS: Crystal Structures, Miissbauer, Magnetic, and Electrical Behavior*, 1976, vol. 128, pp. 117–128.

4 T. Li, Z. Feng, Q. Hou, H. Wu, K. Wang, J.-Y. Ge, S. Cao, J. Zhang and N.-C. Yeh, Effects of Cr doping on the superconductivity and magnetism of $FeTe_{0.8}S_{0.2}$, *Solid State Commun.*, 2020, **309**, 113846, DOI: **10.1016/j.ssc.2020.113846**.

5 P. Paul, A. K. Rajarajan, S. Kuila, P. N. Vishwakarma, B. Mandal and T. V. C. Rao, Plausible Multiferroic and Magneto-Electric Behaviour of Polycrystalline $Bi_{0.85}Gd_{0.05}La_{0.1}FeO_3$ at Room Temperature, *J. Magn. Magn. Mater.*, 2021, **538**, 168253, DOI: **10.1016/j.jmmm.2021.168253**.

6 J. Chen, L. Liu, X. L. Zhu, Z. V. Gareeva, A. K. Zvezdin and X. M. Chen, The Involvement of Pna 2_1 Phase in the Multiferroic Characteristics of La/Lu Co-Substituted BiFeO3 Ceramics, *Appl. Phys. Lett.*, 2021, **119**(11), 112901, DOI: **10.1063/5.0059793**.

7 P. Augustine, N. Yerol, N. Kalarikkal, B. Raneesh, M. T. Rahul and S. K. Chacko, Room Temperature Multiferroic Properties of $BiFeO_3$–$MnFe_2O_4$ Nanocomposites, *Ceram. Int.*, 2021, **47**(11), 15267–15276, DOI: **10.1016/j.ceramint.2021.02.090**.

8 H. Lin, B.-X. Li, H. Chen, P.-F. Liu, L.-M. Wu, X.-T. Wu and Q.-L. Zhu, $Sr_5ZnGa_6S_{15}$: A New Quaternary Non-Centrosymmetric Semiconductor with a 3D Framework Structure Displaying Excellent Nonlinear Optical Performance, *Inorg. Chem. Front.*, 2018, **5**(6), 1458–1462, DOI: **10.1039/C8QI00322J**.

9 R.-H. Duan, J.-S. Yu, H. Lin, Y.-J. Zheng, H.-J. Zhao, S.-X. Huang-Fu, M. A. Khan, L. Chen and L.-M. Wu, $Pb_5Ga_6ZnS_{15}$: A Noncentrosymmetric Framework with Chains of T2-Supertetrahedra, *Dalton Trans.*, 2016, **45**(31), 12288–12291, DOI: **10.1039/C6DT02404A**.

10 B. W. Rudyk, S. S. Stoyko and A. Mar, Rare-Earth Transition-Metal Indium Sulphides RE3FeInS7 (RE=La–Pr), RE3CoInS7 (RE=La, Ce), and La3NiInS7, *J. Solid State Chem.*, 2013, **208**, 78–85, DOI: **10.1016/j.jssc.2013.09.035**.

11 S. Balijapelly, A. J. Craig, J. Bin Cho, J. I. Jang, K. Ghosh, J. A. Aitken, A. V. Chernatynskiy and A. Choudhury, Building-Block Approach to the Discovery of Na8Mn2 (Ge2Se6)2: A Polar Chalcogenide Exhibiting Promising Harmonic Generation Signals with a High Laser-Induced Damage Threshold, *J. Alloys Compd.*, 2022, **900**, 163392, DOI: **10.1016/j.jallcom.2021.163392**.

12 K. Feng, X. Zhang, W. Yin, Y. Shi, J. Yao and Y. Wu, New Quaternary Rare-Earth Chalcogenides Ba Ln Sn 2 Q 6 (Ln = Ce, Pr, Nd, Q = S; Ln = Ce, Q = Se): Synthesis, Structure, and Magnetic Properties, *Inorg. Chem.*, 2014, **53**(4), 2248–2253, DOI: **10.1021/ic402934m**.

13 B. J. Campbell, H. T. Stokes, D. E. Tanner and D. M. Hatch, ISODISPLACE: A Web-Based Tool for Exploring Structural Distortions, *J. Appl. Crystallogr.*, 2006, **39**, 607–614.

14 K. Momma and F. Izumi, VESTA 3 for Three-Dimensional Visualization of Crystal, Volumetric and Morphology Data, *J. Appl. Crystallogr.*, 2011, **44**(6), 1272–1276, DOI: **10.1107/S0021889811038970**.

15 P. E. Blöchl, Projector Augmented-Wave Method, *Phys. Rev. B: Condens. Matter Mater. Phys.*, 1994, **50**(24), 17953–17979, DOI: **10.1103/PhysRevB.50.17953**.

16 G. Kresse and D. Joubert, From Ultrasoft Pseudopotentials to the Projector Augmented-Wave Method, *Phys. Rev. B: Condens. Matter Mater. Phys.*, 1999, **59**(3), 1758–1775, DOI: **10.1103/PhysRevB.59.1758**.

17 G. Kresse, *et al.*, *Vienna Ab-Initio Simulation Package (VASP)*.

18 J. P. Perdew, K. Burke and M. Ernzerhof, Generalized Gradient Approximation Made Simple, *Phys. Rev. Lett.*, 1996, **77**(18), 3865–3868, DOI: **10.1103/PhysRevLett.77.3865**.

19 V. Petříček, M. Dušek and L. Palatinus, Crystallographic Computing System JANA2006: General Features, *Z. Kristallogr. – Cryst. Mater.*, 2014, **229**(5), 345–352, DOI: **10.1515/zkri-2014-1737**.

20 A. van der Lee, Charge Flipping for Routine Structure Solution, *J. Appl. Crystallogr.*, 2013, **46**(5), 1306–1315, DOI: **10.1107/S0021889813020049**.

21 S. Cohen, N. Kimizuka and H. Steinfink, The Crystal Structure and Stability of Ba5Fe4S11, *J. Solid State Chem.*, 1980, **35**(2), 181–186, DOI: **10.1016/0022-4596(80)90491-0**.

22 W. Yin, A. K. Iyer, C. Li, J. Yao and A. Mar, $Ba_5CdGa_6Se_{15}$, a Congruently-Melting Infrared Nonlinear Optical Material with Strong SHG Response, *J. Mater. Chem. C*, 2017, **5**(5), 1057–1063, DOI: **10.1039/C6TC05111A**.

23 J. M. Perez-Mato, D. Orobengoa and M. I. Aroyo, Mode Crystallography of Distorted Structures, *Acta Crystallogr., Sect. A: Found. Crystallogr.*, 2010, **66**(5), 558–590, DOI: **10.1107/S0108767310016247**.

24 J. K. Shenton, D. R. Bowler and W. L. Cheah, Effects of the Hubbard U on Density Functional-Based Predictions of $BiFeO_3$ Properties, *J. Phys.: Condens. Matter*, 2017, **29**(44), 445501, DOI: **10.1088/1361-648X/aa8935**.

25 X. Li, H. Yu, F. Lou, J. Feng, M.-H. Whangbo and H. Xiang, Spin Hamiltonians in Magnets: Theories and Computations, *Molecules*, 2021, **26**(4), 803, DOI: **10.3390/molecules26040803**.

26 L. Duan, J. Zhang, X. Wang, Z. Zhao, C. Xiao, X. Li, Z. Hu, J. Zhao, W. Li, L. Cao, G. Dai, C. Ren, X. He, R. Yu, Q. Liu, L. H. Tjeng, H.-J. Lin, C.-T. Chen and C. Jin, High Pressure Phase of $Ba2FeS_3$: An Antiferromagnet with One-Dimensional Spin Chains, *J. Alloys Compd.*, 2021, **859**, 157839, DOI: **10.1016/j.jallcom.2020.157839**.

27 J. S. Swinnea and H. Steinfink, Mössbauer Spectra, Magnetic and Electrical Behavior of Ba1+xFe2S4 Phases, *J. Solid State Chem.*, 1982, **41**(2), 124–131, DOI: **10.1016/0022-4596(82)90192-X**.